IJMMM International Journal of Minerals, Metallurgy and Materials 矿物冶金与材料学报（英文版）

Comprehensive utilization of solid waste resources: Development of wet shotcrete for mines

Yafei Hu, Shenghua Yin, Keqing Li, Bo Zhang, and Bin Han

Cite this article as:
Yafei Hu, Shenghua Yin, Keqing Li, Bo Zhang, and Bin Han, Comprehensive utilization of solid waste resources: Development of wet shotcrete for mines, *Int. J. Miner. Metall. Mater.*, 30(2023), No. 9, pp. 1692-1704. https://doi.org/10.1007/s12613-022-2563-8

View the article online at SpringerLink or IJMMM Webpage.

International Journal of Minerals, Metallurgy and Materials
Volume 30, Number 9, September 2023, Page 1692
https://doi.org/10.1007/s12613-022-2563-8

Comprehensive utilization of solid waste resources: Development of wet shotcrete for mines

Yafei Hu[1,2], *Shenghua Yin*[1,2], *Keqing Li*[1,2], *Bo Zhang*[1,2], *and Bin Han*[1,2)✉]

1) School of Civil and Resource Engineering, University of Science and Technology Beijing, Beijing 100083, China
2) Key Laboratory of Ministry of Education of China for Efficient Mining and Safety of Metal Mines, University of Science and Technology Beijing, Beijing 100083, China
(Received: 28 August 2022; revised: 23 October 2022; accepted: 24 October 2022)

Abstract: The development of solid waste resources as constituent materials for wet shotcrete has significant economic and environmental advantages. In this study, the concept of using tailings as aggregate and fly ash and slag powder as auxiliary cementitious material is proposed and experiments are carried out by response surface methodology (RSM). Multivariate nonlinear response models are constructed to investigate the effect of factors on the uniaxial compressive strength (UCS) of tailings wet shotcrete (TWSC). The UCS of TWSC is predicted and optimized by constructing Gaussian process regression (GPR) and genetic algorithm (GA). The UCS of TWSC is gradually enhanced with the increase of slag powder dosage and fineness modulus, and it is enhanced first and then decreased with the increase of fly ash dosage. The microstructure of TWSC has the highest gray value and the highest UCS when the fly ash dosage is about 120 kg·m^{-3}. The GPR–GA model constructed in this study achieves high accuracy prediction and optimization of the UCS of TWSC under multi-factor conditions.

Keywords: tailings; solid waste; wet shotcrete; machine learning; mix proportion

1. Introduction

Tailings are generally deposited on the surface and contain heavy metals [1–3]. After scientific research, the tailings are successfully filled into the underground mining area [4–11]. However, the quantity of tailings generated by mines are much more than the quantity of tailings required for filling [12–13]. In order to improve the utilization rate of tailings, this study proposes the concept of using tailings as aggregate to replace sand and gravel in wet shotcrete.

In order to optimize the strength of tailings wet shotcrete (TWSC) and reduce the cement dosage, solid waste materials such as slag powder and fly ash are considered to be added to binder and form a composite cementitious system with cement [14–20]. Relevant studies show that slag powder and fly ash have the potential to replace part of cement as auxiliary cementitious material [21–22]. Fly ash plays a critical role in improving the fluidity of concrete due to its fineness, ball effect, and less water requirement [23]. Slag powder is a potential auxiliary cementitious material. In the early stage of hydration, it will reduce the compactness of cemented paste structure in different degree [24].

Machine learning techniques have also been used in studies related to concrete strength optimization. Related scholars have carried out uniaxial compressive strength (UCS) prediction of concrete using support vector regression (SVR), decision trees (DT), random forests (RF), back propagation neural networks (BPNN), and extreme learning machines (ELM) [9,25–29]. By training and validating the models, high prediction accuracy is achieved. In addition, optimization methods such as genetic algorithms (GA) and particle swarm optimization (PSO) can be used to calculate the ratio of the corresponding materials based on the required concrete strength [30–32].

In this study, response surface methodology (RSM) is used to design the experiments and construct the strength response model of tailings wet shotcrete (TWSC). The microstructure analysis of TWSC is also carried out by scanning electron microscope (SEM). In addition, a Gaussian process regression (GPR) model is constructed to predict the strength of TWSC and GA is used to optimize the mix proportion of TWSC.

2. Materials and methods

2.1. Materials

2.1.1. Tailings

The main chemical composition of the tailings are shown in Table 1. The activity coefficient of the tailings is calculated to be M_a = 0.037, which indicates its suitability for use as an aggregate. The X-ray diffraction (XRD) test results of the tailings are shown in Fig. 1(a).

✉ Corresponding author: Bin Han E-mail: bin.han@ustb.edu.cn

Table 1. Main chemical composition of the tailings wt%

SiO_2	CaO	MgO	Fe_2O_3	Al_2O_3	MnO	SO_3	TiO_2
67.1	2.51	0.65	2.17	16.73	0.15	0.9	0.25

In order to study the effect of different particle size of tailings on the UCS of wet shotcrete, the hydraulic cyclone is used to classify the tailings and obtain 3 different grades of graded tailings. To better quantify the particle size distribution of the tailings, the fineness modulus is introduced to quantitatively characterize the coarseness and fineness of the tailings with reference to the definitions of the fineness modulus of coarse sand in the relevant industries. Define the fineness modulus of the tailings as follows:

$$\mathrm{MX} = \frac{\sum_{i=1}^{5} A_i - 5A_6}{100 - A_6} \tag{1}$$

where A_i is the percentage of sieve residue for standard sieves of 2 μm, 10 μm, 30 μm, 75 μm, 300 μm, and 700 μm, wt%; MX is the fineness modulus.

The particle sizes of the tailings measured with the laser granularity analyzer are shown in Fig. 1(b). In this figure, d_{50} represents the median particle size of the tailings (μm), while Cu represents the coefficient of uniformity of the tailings. Using Eq. (1), the fineness moduli of the 3 tailings are obtained as 2.96, 3.53, and 4.02, respectively.

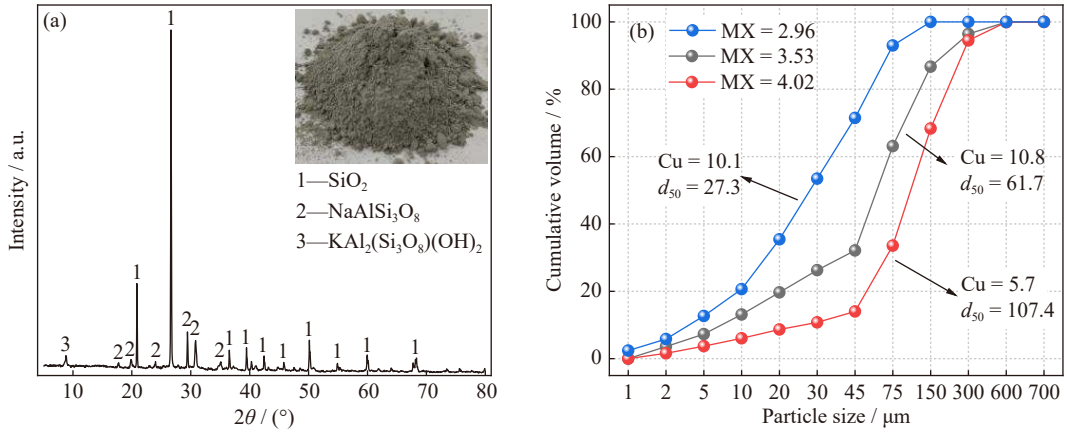

Fig. 1. XRD test results (a) and particle size distribution (b) of tailings.

2.1.2. Cementitious materials

This paper uses cement, fly ash, and slag powder to make a composite cementitious material. Cement is the activator and fly ash and slag powder are the active materials. The physical and chemical characteristics of each material are as follows.

(1) PO42.5 grade silicate cement is used as the main cementitious material, and it has a density of 3.03 g·cm^{-3}, and 28-d compressive and flexural strengths of 54.3 and 8.7 MPa, respectively.

(2) Fly ash is the main solid particulate waste emitted from coal-fired power plants. Its density is 2.55 g·cm^{-3} and specific surface area is 0.35 m^2·kg^{-1}. From XRD analysis, it is clear that fly ash mainly contains mineral phases such as mullite, quartz, and alumina.

(3) Slag powder is granulated blast furnace slag. It has a specific surface area of 440 m^2·kg^{-1} and a density of 2.9 g·cm^{-3}. In addition, it has an alkalinity coefficient of M_0 = 1.17 > 1, a quality coefficient of K = 2.27 > 1.8, and an activity coefficient of M_a = 1.57. This indicates that the slag powder is a highly reactive alkaline slag. The chemical and particle size compositions of cementitious materials are shown in Table 2 and Fig. 2, respectively.

2.2. Methods

2.2.1. Experimental design

In order to obtain the variation law of the UCS of TWSC under the coupling effect of multiple factors and to effectively improve the experimental efficiency, the RSM in Design-Expert software is used to optimize the experimental design [33–35]. RSM experiments are conducted with fly ash dosage (80–160 kg·m^{-3}), slag powder dosage (30–90 kg·m^{-3}), and fineness modulus (3–4) as independent variables, denoted by X_1, X_2, and X_3, respectively. The 7 d, 14 d, and 28 d UCS of TWSC are used as the response quantity and are expressed as Y_1, Y_2, and Y_3, respectively. The RSM experimental protocol is shown in Table 3.

2.2.2. Test methods

The main test methods are UCS test and SEM test, and the two tests are described below.

UCS is the key mechanical parameter of TWSC. For comparison, the three important variables in the 17 groups of experiments in this research, i.e., fly ash dosage, slag powder dosage, and fineness modulus are listed in Table 4. The fixed dosage of cement in the cementitious materials is 460 kg·m^{-3}. The materials were weighed according to the proportion of each group of experiments, then the materials were poured into a bucket and mixed for 5 min using a hand-held electric

Table 2. Chemical compositions of the cementitious materials wt%

Material	SiO_2	CaO	MgO	Fe_2O_3	Al_2O_3	SO_3
Cement	20.35	62.20	4.22	3.17	4.34	2.54
Fly ash	45.10	5.60	1.13	0.85	24.20	2.10
Slag powder	27.51	43.24	8.09	0.38	16.25	1.51

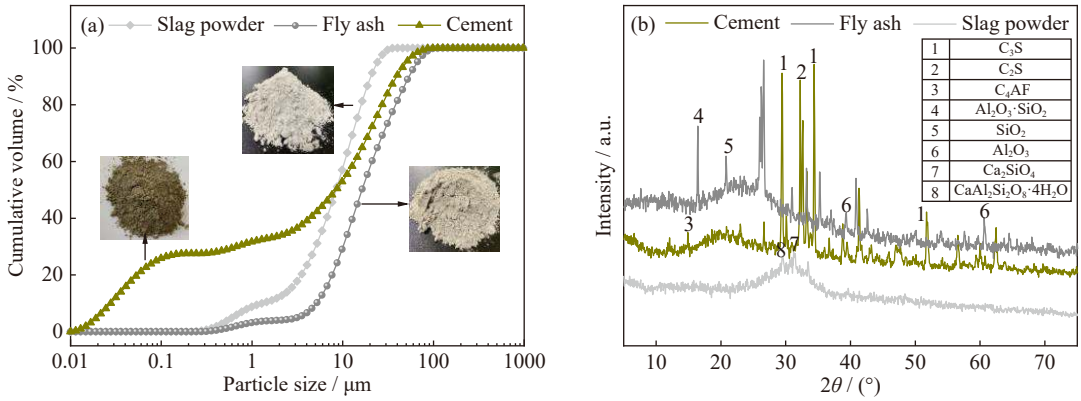

Fig. 2. Particle size distributions (a) and XRD test results (b) of the cementitious materials.

Table 3. RSM experimental protocol

Horizontal code	Fly ash dosage (X_1) / (kg·m^{-3})	Slag powder dosage (X_2) / (kg·m^{-3})	Fineness modulus (X_3)
−1	80	30	3.0
0	120	60	3.5
1	160	90	4.0

mixer. The mixed slurry was poured into a triplex test mold of size 100 mm × 100 mm × 100 mm, and then vibrated for 2 min on a vibrating table of model ZS-15 to improve the compactness of the materials. The prepared specimens were put into the standard curing box for curing. The curing temperature is set to 20°C and the curing humidity is set to 95%. After waiting for the specimens to be cured to 7, 14, and 28 d, the automatic pressure testing machine was used for UCS tests.

SEM method has been widely used to analyze the microstructural of concrete and its components since the 1960s, and it is recommended as a standard by ASTM to study concrete and who are familiar [36–38]. The TWSC is a cement-based material used in mines, and its micro-properties are often tested by SEM. As shown in Fig. S1, a Quanta FEG 250 field-emission electron microscopy system with an accelerating voltage of 10 kV is used to test the specimens of TWSC without the UCS test, and the influence of multiple factors on the microstructural properties of the TWSC is studied.

2.3. RSM Results and response models

The results of RSM experiments are shown in Table 4.

17 sets of experimental results in Table 4 are fitted with a multivariate nonlinear model to construct a response model for the UCS of TWSC at different curing time. The response models are shown in Eqs. (2)–(4).

(1) 7 d UCS

$$Y_1^* = 13.07 + 0.15X_1 + 0.07X_2 - 6.63X_3 - (8.96\times10^{-5})X_1X_2 + (6.45\times10^{-3})X_1X_3 + (2.87\times10^{-3})X_2X_3 - (6.81\times10^{-4})X_1^2 - (1.60\times10^{-4})X_2^2 + 1.06X_3^2,\ R^2 = 0.96 \quad (2)$$

Table 4. Results of RSM experiments

Group number	Factors			Measured value / MPa			Predicted value / MPa		
	X_1 / (kg·m^{-3})	X_2 / (kg·m^{-3})	X_3	Y_1	Y_2	Y_3	Y_1^*	Y_2^*	Y_3^*
1	120	60	3.55	16.82	18.60	20.67	16.98	18.64	20.65
2	120	90	3.0	17.51	19.68	21.68	17.73	19.42	21.50
3	80	60	3.0	15.79	17.35	18.95	15.40	17.23	18.79
4	120	60	3.5	17.00	18.72	20.80	16.98	18.64	20.65
5	80	60	4.0	16.57	19.17	20.97	16.86	19.15	20.87
6	120	60	3.5	17.08	18.72	20.84	16.98	18.64	20.65
7	160	30	3.5	14.50	15.98	17.48	14.34	15.61	17.18
8	120	60	3.5	16.82	18.83	20.76	16.98	18.64	20.65
9	160	90	3.5	17.08	18.94	21.09	17.20	18.99	21.02
10	80	30	3.5	14.16	15.64	17.06	14.08	15.41	16.86
11	80	90	3.5	17.17	19.00	21.22	17.37	19.19	21.22
12	120	90	4.0	20.01	22.14	23.99	19.54	21.77	23.69
13	160	60	4.0	16.74	19.40	21.22	17.16	19.35	21.10
14	120	60	3.5	17.08	18.72	20.88	16.98	18.64	20.65
15	120	30	4.0	16.57	17.86	19.75	16.38	17.96	19.65
16	120	30	3.0	14.24	15.87	17.31	14.74	16.07	17.34
17	160	60	3.0	15.45	17.18	18.87	15.19	17.03	18.68

Note: Y_1^*, Y_2^*, and Y_3^* denote the predicted values of UCS at 7 d, 14 d, and 28 d, respectively.

(2) 14 d UCS

$$Y_2^* = 26.33 + 0.13X_1 + 0.09X_2 - 13.69X_3 - (8.31\times10^{-5})X_1X_2 + (4.99\times10^{-3})X_1X_3 + (7.60\times10^{-3})X_2X_3 - (6.06\times10^{-4})X_1^2 - (3.96\times10^{-4})X_2^2 + 2.11X_3^2,\ R^2 = 0.99 \quad (3)$$

(3) 28 d UCS

$$Y_3^* = 13.76 + 0.16X_1 + 0.15X_2 - 7.63X_3 - (1.14\times10^{-4})X_1X_2 + (4.20\times10^{-3})X_1X_3 - (2.10\times10^{-3})X_2X_3 - (7.06\times10^{-4})X_1^2 - (4.97\times10^{-4})X_2^2 + 1.36X_3^2,\ R^2 = 0.99 \quad (4)$$

The UCSs of TWSC are predicted based on the above models and the predicted results are shown in Table 4 and Fig. 3. The widest prediction and confidence bands in Fig. 3(a) and the narrowest prediction and confidence bands in Fig. 3(c) indicate that the 28 d UCS response model has the highest prediction accuracy and the 7 d UCS response model has the lowest prediction accuracy. The UCS calculated by response models all lie within the 95% prediction band and are close to the 95% confidence band. This indicates that the response models have a high reliability.

3. Analysis and discussion

3.1. Effect of single factor on UCS

3.1.1. Fly ash dosage

The relationship between fly ash dosage and UCS is shown in Fig. 4. With the increase of fly ash dosage, the UCS first increases and then decreases. When the fly ash dosage is lower than 120 kg·m^{-3}, the UCS increases with the increase of fly ash dosage but the increase rate gradually decreases. When the fly ash dosage is higher than 120 kg·m^{-3}, the UCS decreases with the increase of fly ash dosage and the decrease is more significant. Overall, the increase and decrease rates of 7 d UCS are both higher than 14 d UCS and 28 d UCS. This indicates that the fly ash dosage has a more significant effect on the early UCS of TWSC. Fly ash undergoes volcanic ash reaction in the composite cementitious system, which consumes $Ca(OH)_2$ that is unfavorable to early strength and thus promotes the hydration reaction, so fly ash has the most significant effect on the early UCS of TWSC. However, when the fly ash dosage is too high, it will lead to pore space between the solid particles of TWSC and reduce its UCS.

3.1.2. Slag powder dosage

The relationship between slag powder dosage and UCS is shown in Fig. 5. With the increase of slag powder dosage, the UCS gradually increases but the increase rate gradually decreases. The increase rates of 14 d UCS and 28 d UCS are higher than 7 d UCS when the slag powder dosage is lower than 80 kg·m^{-3}. Within this range, the maximum increase rates of 14 d UCS and 28 d UCS are increased by up to 25.6% and 33.3% compared to 7 d UCS. The increase rates of both 14 d UCS and 28 d UCS are lower than 7 d UCS when the slag powder dosage is higher than 80 kg·m^{-3}. Meanwhile, the decrease of UCS is increasing with the increase of slag powder dosage. The above results show that when the slag powder dosage is lower than 80 kg·m^{-3}, the slag powder dosage has the most significant effect on the

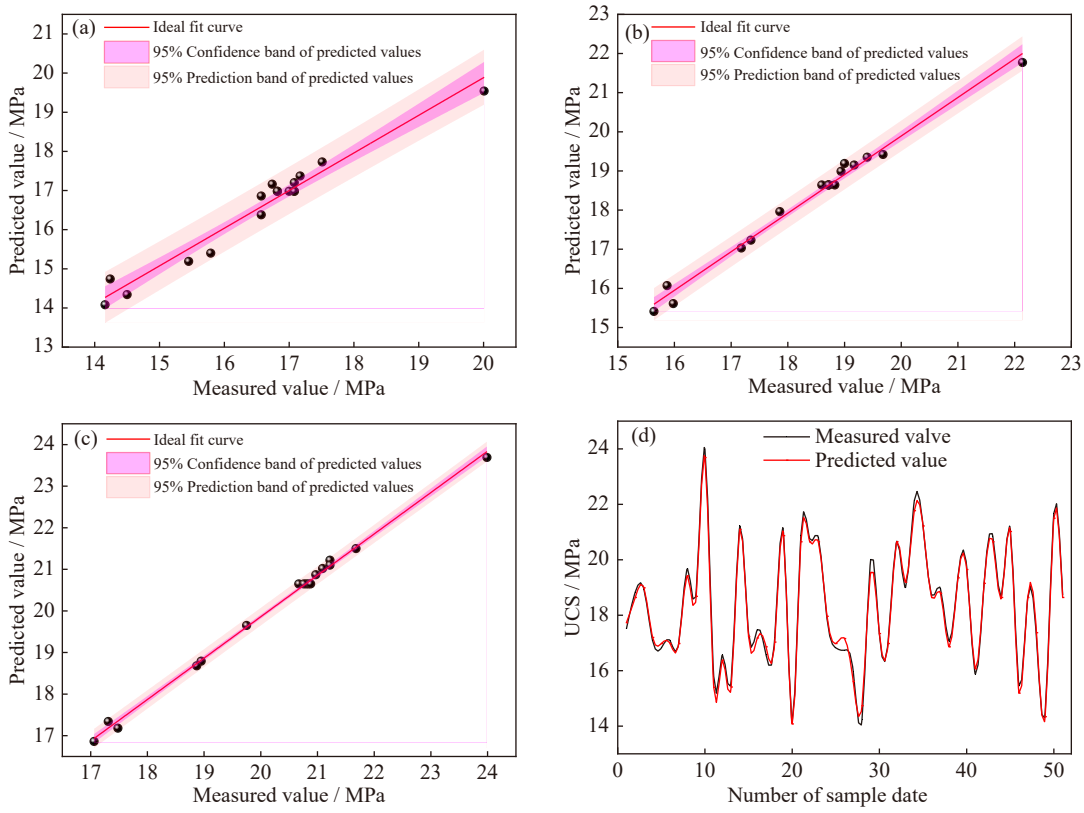

Fig. 3. Predicted and measured results of (a) 7 d UCS, (b) 14 d UCS, (c) 28 d UCS, and (d) all UCS.

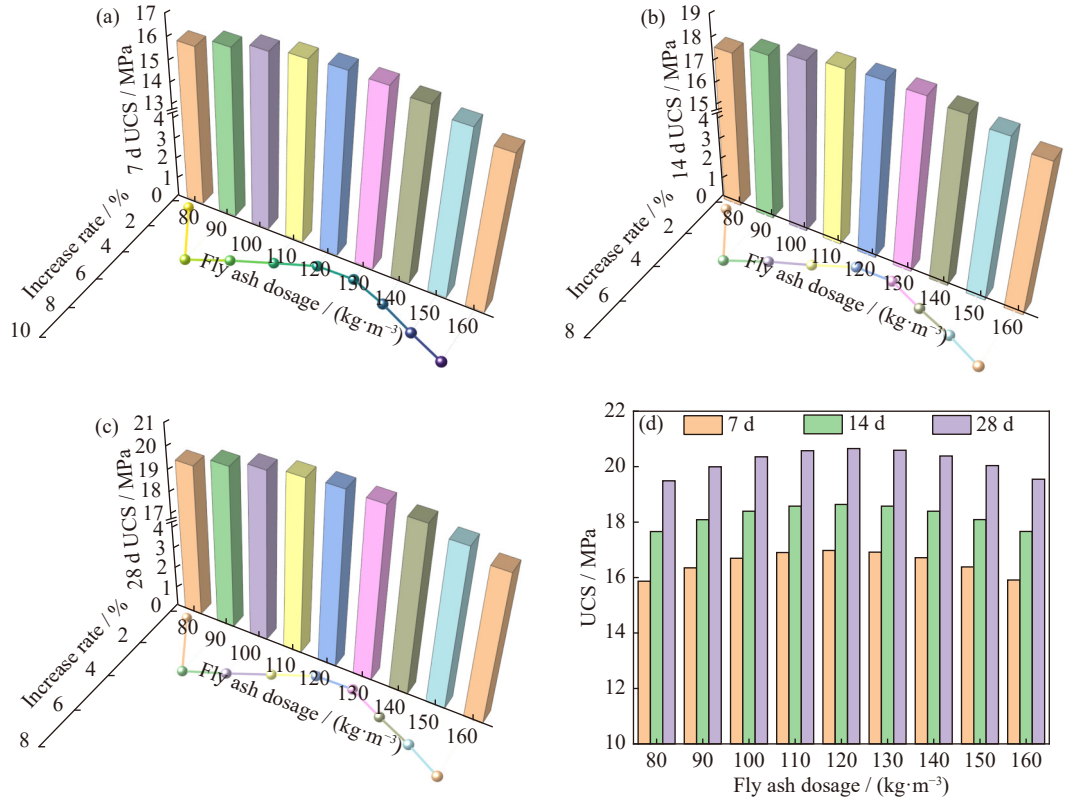

Fig. 4. Relationship between fly ash dosage and UCS: (a) 7 d UCS; (b) 14 d UCS; (c) 28 d UCS; (d) all UCS.

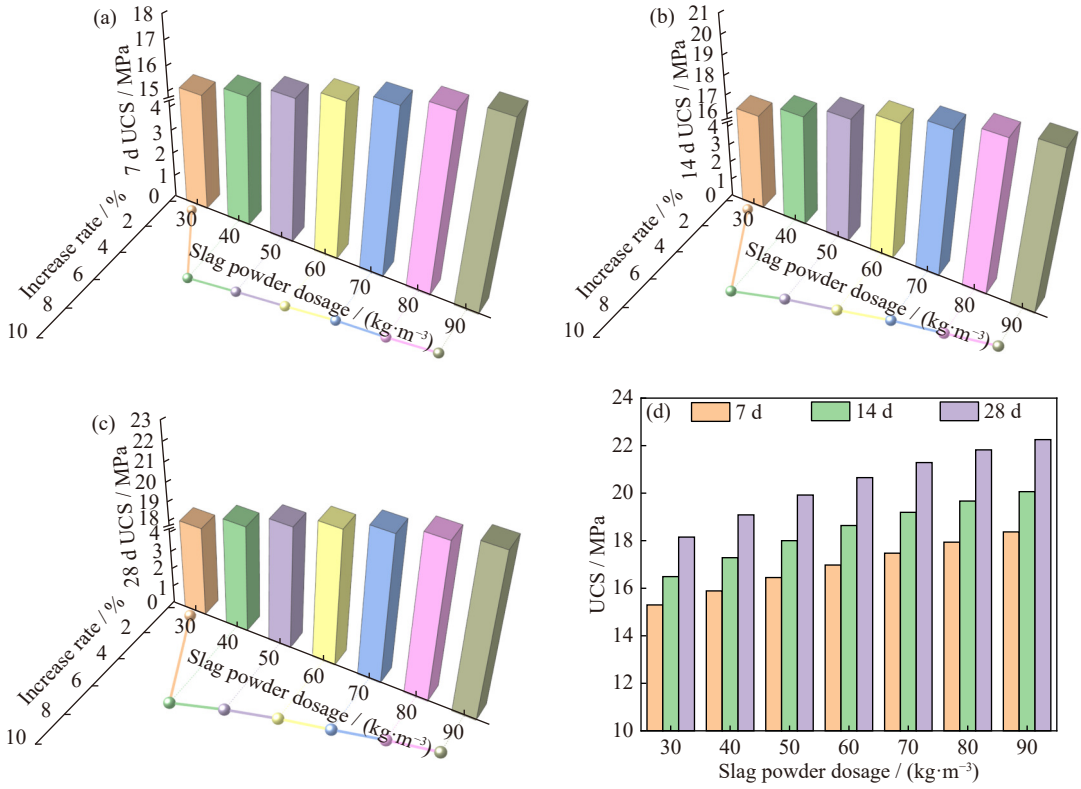

Fig. 5. Relationship between slag powder dosage and UCS: (a) 7 d UCS; (b) 14 d UCS; (c) 28 d UCS; (d) all UCS.

UCS of TWSC in the middle and late stages. When the slag powder dosage is more than 80 kg·m^{-3}, the slag powder dosage has the most significant effect on the UCS of TWSC in the early stage. The $Ca(OH)_2$ generated by cement hydration can stimulate the "potential activity" of slag powder and produce more calcium silicate hydrate (C–S–H) gel, which can improve the UCS of TWSC. Therefore, the UCS of TWSC increases with the increase of slag powder dosage.

3.1.3. Fineness modulus

The relationship between fineness modulus and UCS is

shown in Fig. 6. With the increase of fineness modulus, the UCS is gradually increased and the increase rate is increasing. When the fineness modulus is less than 3.4, the increase rate of 28 d UCS is the highest, 7 d UCS is second, and 14 d UCS is the lowest. When the fineness modulus is higher than 3.4, the increase rate of 14 d UCS is the highest, 28 d UCS is second, and 7 d UCS is the lowest. The above results show that when the fineness modulus is lower than 3.4, the fineness modulus has the most significant effect on the UCS in later stage and the least effect on UCS in middle stage. When the fineness modulus is higher than 3.4, the fineness modulus has the most significant effect on the UCS in middle stage and the least effect on the UCS in early stage. The particle size of ultrafine tailings is small overall, and increasing its fineness modulus means more coarse particles in the tailings. The coarse particles can provide a skeleton structure for TWSC and the fine particles fill the skeleton, which makes the structure of TWSC more compact and thus improves its UCS.

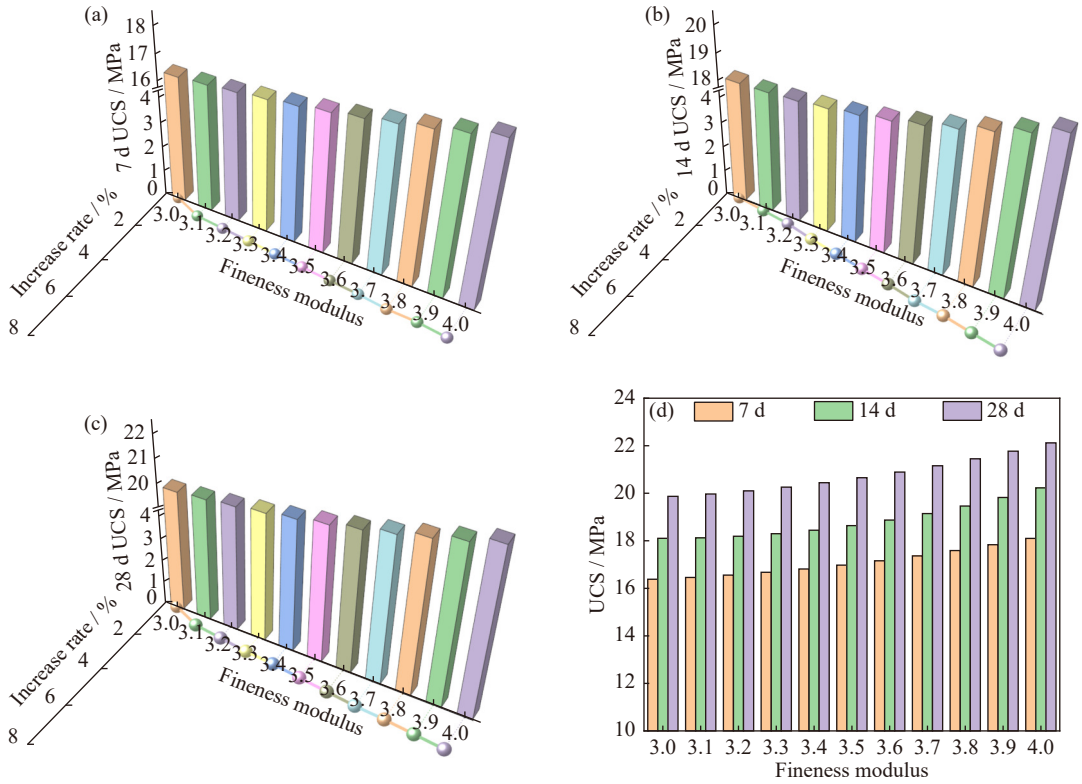

Fig. 6. Relationship between fineness modulus and UCS: (a) 7 d UCS; (b) 14 d UCS; (c) 28 d UCS; (d) all UCS.

3.2. Coupling effect of multi-factor on UCS

3.2.1. Coupling effect of fly ash dosage and fineness modulus

The coupling effect of fly ash dosage and fineness modulus on UCS is shown in Fig. 7. When the fineness modulus is lower than 3.5, the response surface slowly rises in the direction of this axis. When the fineness modulus is higher than 3.5, the response surface rises rapidly along the direction of this axis. In addition, the UCS enhances and then decreases with the increase of fly ash dosage. The UCS has a maxim-

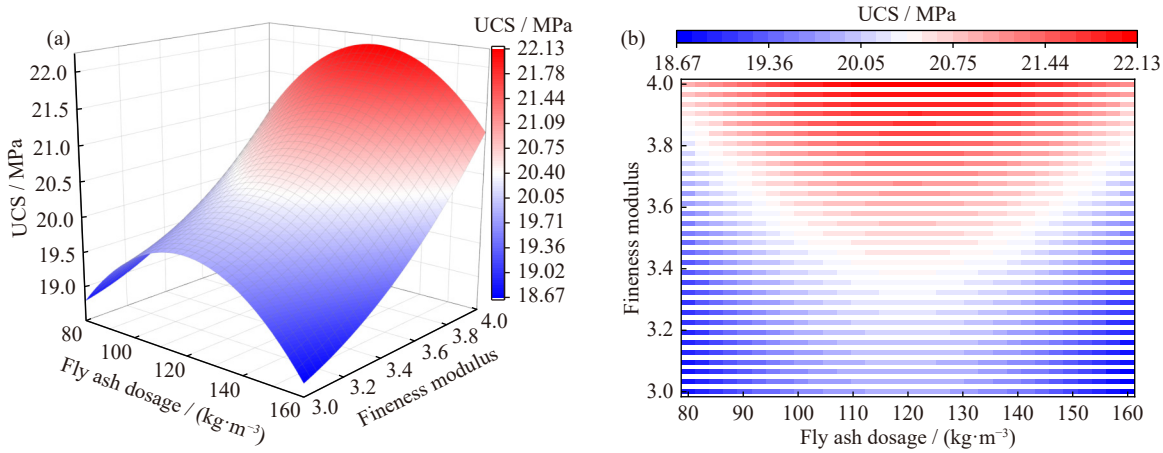

Fig. 7. Coupling effect of fly ash dosage and fineness modulus on (a) UCS and (b) response surface contour.

um value of 22.13 MPa when the fly ash dosage is 121 kg·m^{-3} and the fineness modulus is 4. The reasons are analyzed as follows. The higher the fineness modulus is, the particle size of tailings is, at this time the fly ash particles without hydration reaction form an embedded lock structure with coarse sand particles, which makes the UCS enhance.

3.2.2. Coupling effect of slag powder dosage and fineness modulus

The coupling effect of slag powder dosage and fineness modulus on UCS is shown in Fig. 8. It can be seen that increasing both the slag powder dosage and the fineness modulus can significantly enhance the UCS. The UCS is enhanced by 24.3% when the fineness modulus is 3 and the slag powder dosage is increased from 30 to 90 kg·m^{-3}. The UCS is enhanced by 20.9% when the fineness modulus is 4 and the slag powder dosage is increased from 30 to 90 kg·m^{-3}. The above results show that the enhancement of UCS by slag powder is more significant when the particle size of tailings is finer (lower fineness modulus).

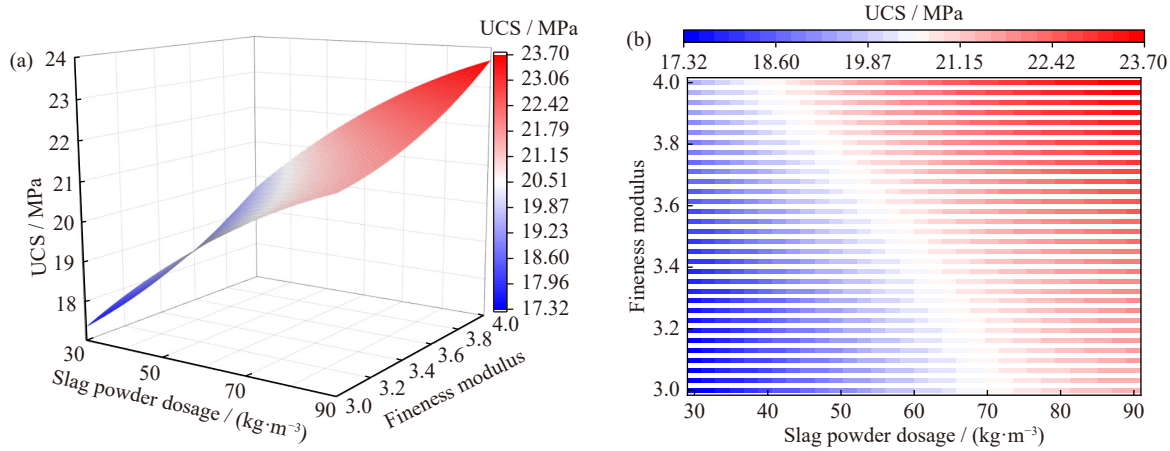

Fig. 8. Coupling effect of slag powder dosage and fineness modulus on (a) UCS and (b) response surface contour.

3.2.3. Coupling effect of slag powder dosage and fly ash dosage

The coupling effect of fly ash dosage and slag powder dosage on UCS is shown in Fig. 9. It can be seen that the UCS is enhanced with the increase of slag powder dosage at any fly ash dosage. The UCS is enhanced and then decreased with the increase of fly ash dosage at any slag powder dosage. In the process of increasing the fly ash dosage from 80 to 160 kg·m^{-3}, the increase rate of UCS shows a trend of decreasing and then increasing with the increase of slag powder dosage. This trend is opposite to the trend of UCS. The UCS reached the maximum value of 22.26 MPa when the fly ash dosage is 119 kg·m^{-3} and the slag powder dosage is 90 kg·m^{-3}.

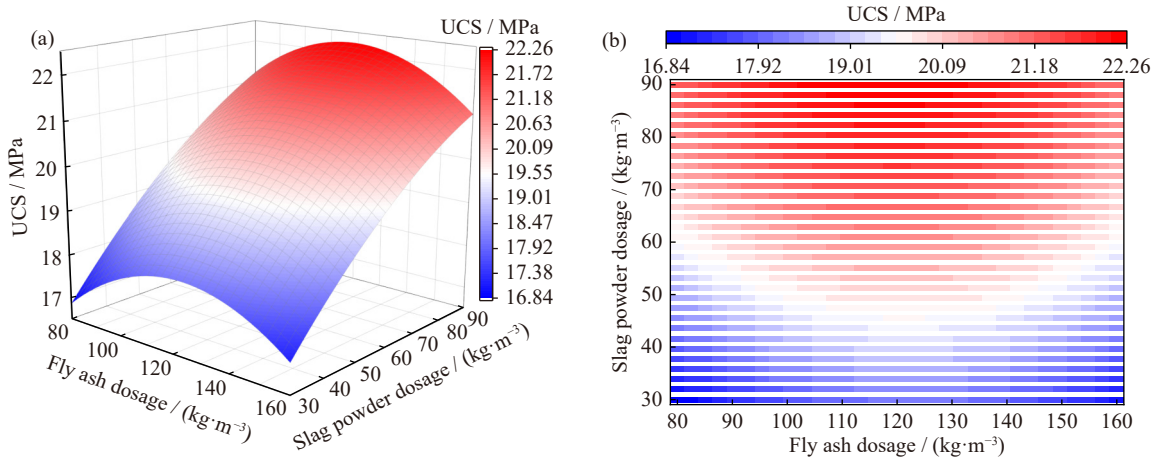

Fig. 9. Coupling effect of fly ash dosage and slag powder dosage on (a) UCS and (b) response surface contour.

3.3. Microscopic analysis

The microstructure images of TWSC are obtained by SEM and the images are binarized by Image J software. The final 2D and 3D gray images of the microstructure are obtained as shown in Fig. 10. A large number of substances such as C–S–H gels and ettringite (AFt) crystals are produced by hydration reaction. The needle-like AFt crystals are interwoven to form a network structure and are wrapped by the C–S–H gels to fill the pore space. And then, the solid particles are bonded together to form a cemented structure, which gives strength to the TWSC.

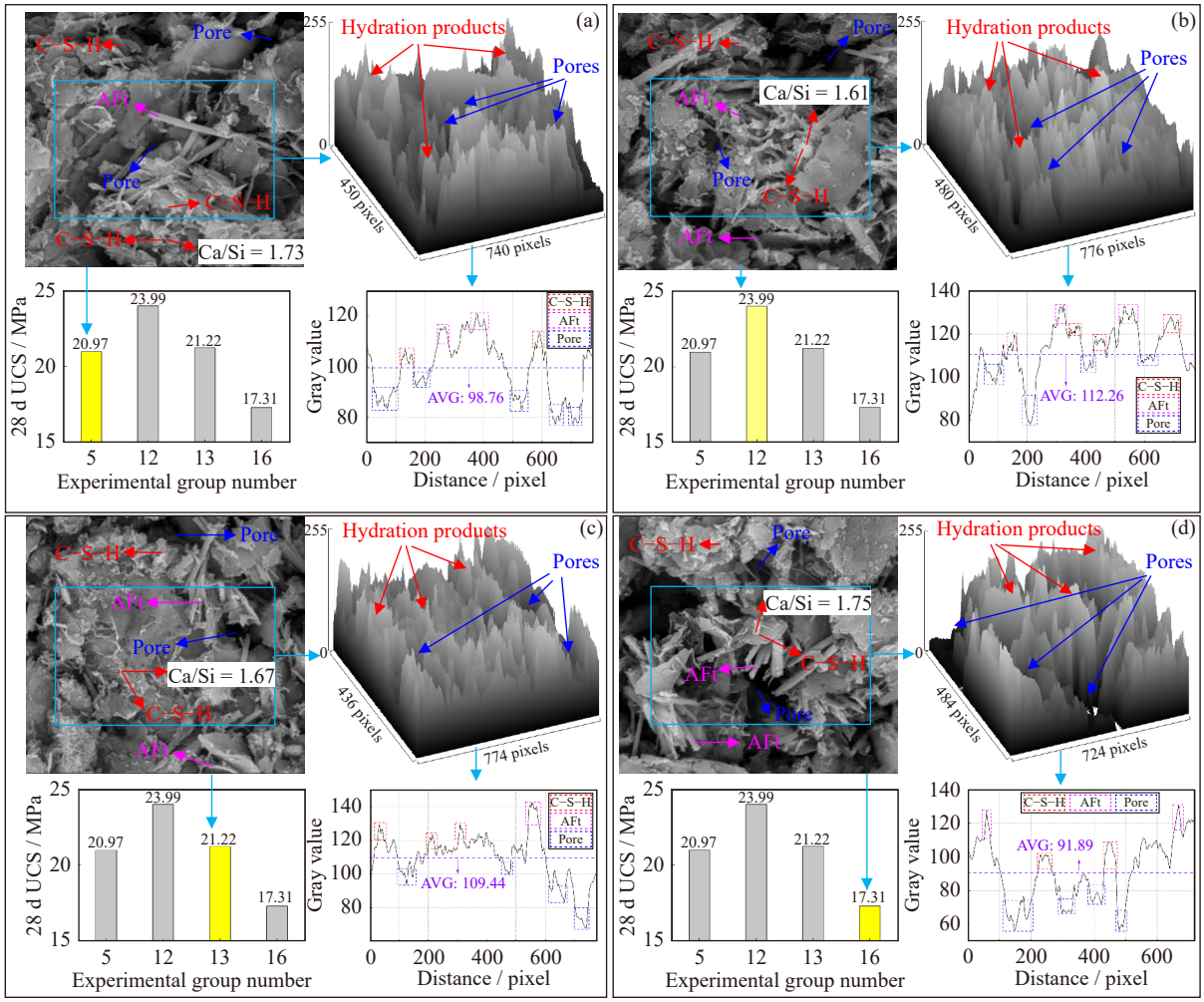

Fig. 10. Microstructure and gray scale diagram of TWSC: (a) group 5; (b) group 12; (c) group 13; (d) group 16.

Comparing Fig. 10(a), (b), and (c), it can be seen that the average grey value increases from 98.76 and 109.44 to 112.26 when the fly ash dosage changes from 80 and 160 to 120 kg·m^{-3}, respectively. Meanwhile, the 28 d UCS enhances from 20.97 and 21.22 to 23.99 MPa. This indicates that an appropriate fly ash dosage can improve the grey value of the microstructure of TWSC, which is expressed macroscopically as an increase in the UCS of TWSC. The Ca/Si (C/S) mass ratio of C–S–H gels in TWSC were 1.73 and 1.67 when the fly ash dosage was 80 and 160 kg·m^{-3}, respectively, and the C/S mass ratio of C–S–H gels in TWSC decreased to 1.61 when the fly ash dosage was 120 kg·m^{-3}. The lower the C/S mass ratio, the higher the stability of C–S–H gels and thus the higher the UCS of TWSC. Comparing Fig. 10(b) and (d), it can be seen that the average grey value increases by 22% when the slag powder dosage and fineness modulus are increased by 200% and 33%, respectively. Meanwhile, the 28 d UCS is enhanced by 39%. This indicates that with the increase of slag powder dosage and fineness modulus, the hydration products increase and the pore space in TWSC decreases, which leads to the enhancement of UCS of TWSC.

4. Methodology of machine learning

In order to obtain the best mix proportion of TWSC rapidly, an intelligent prediction model of strength of TWSC based on GPR is constructed in this study.

4.1. Gaussian process regression

GPR is a nonlinear and Bayesian-based nonparametric inference method that is well-adapted to high-dimensional data and small-sample data [39–42]. A stochastic process is called Gaussian process (GP) if any number of random variables in the process are subject to a multidimensional joint Gaussian distribution. It has the following mathematical expression:

$$f(\boldsymbol{x}) \sim \mathrm{GP}\left[m(\boldsymbol{x}), k(\boldsymbol{x}, \boldsymbol{x}')\right] \tag{5}$$

$$m(\boldsymbol{x}) = E\left[f(\boldsymbol{x})\right] \tag{6}$$

$$k(\boldsymbol{x}, \boldsymbol{x}') = E\left\{\left[f(\boldsymbol{x}) - m(\boldsymbol{x})\right]\left[f(\boldsymbol{x}') - m(\boldsymbol{x}')\right]\right\} \tag{7}$$

where $\boldsymbol{x}$ and $\boldsymbol{x}'$ are arbitrary random variables in the s-dimensional real space; $f(\boldsymbol{x})$ is a GP; $m(\boldsymbol{x})$ and $m(\boldsymbol{x}')$ are the mean functions of $f(\boldsymbol{x})$ and $f(\boldsymbol{x}')$, respectively; $k(\boldsymbol{x}, \boldsymbol{x}')$ is the covariance function of $f(\boldsymbol{x})$ and $f(\boldsymbol{x}')$, E is the expectation function.

According to the Bayesian linear regression model, the GP is assumed as $f(\boldsymbol{x}) = \phi(\boldsymbol{x})^{\mathrm{T}}\boldsymbol{w}$. In the above equation, $\boldsymbol{w}$ is the weight function and its prior distribution is subject to $\boldsymbol{w} \sim N(0, \boldsymbol{M}_{\mathrm{P}})$, $E(\boldsymbol{w}) = 0$, and $E(\boldsymbol{w}\boldsymbol{w}^{\mathrm{T}}) = \boldsymbol{M}_{\mathrm{P}}$. From this,

the mean function and covariance function of $f(\boldsymbol{x})$ are as follows:

$$E[f(\boldsymbol{x})] = \phi(\boldsymbol{x})^{\mathrm{T}} E(\boldsymbol{w}) = 0 \tag{8}$$

$$E[f(\boldsymbol{x})f(\boldsymbol{x}')] = \phi(\boldsymbol{x})^{\mathrm{T}} E(\boldsymbol{w}\boldsymbol{w}^{\mathrm{T}})\phi(\boldsymbol{x}') = \phi(\boldsymbol{x})^{\mathrm{T}} M_{\mathrm{P}}\phi(\boldsymbol{x}') \tag{9}$$

where $\boldsymbol{M}_{\mathrm{P}}$ denotes the covariance matrix. Both $f(\boldsymbol{x})$ and $f(\boldsymbol{x}')$ are subject to the joint Gaussian distribution $N[0, \phi(\boldsymbol{x})^{\mathrm{T}} M_{\mathrm{P}}\phi(\boldsymbol{x}')]$. That is, for any n input vectors $\boldsymbol{x}_1$, $\boldsymbol{x}_2$, ..., $\boldsymbol{x}_n$, their corresponding function values $f(\boldsymbol{x}_1)$, $f(\boldsymbol{x}_2)$, $f(\boldsymbol{x}_3)$, ..., $f(\boldsymbol{x}_n)$ all submit to the joint Gaussian distribution $N\left[0, \phi(\boldsymbol{x})^{\mathrm{T}} M_{\mathrm{P}}\phi(\boldsymbol{x}')\right]$.

There are Gaussian noises ε in the actual observations, which are independent of each other and subject to Gaussian distribution $\varepsilon \sim N(0, \sigma^2)$. It follows that $\boldsymbol{y} = f(\boldsymbol{x}) + \varepsilon$ and $\mathrm{cov}(\boldsymbol{y}) = K(\boldsymbol{X}, \boldsymbol{X}) + \sigma_n^2 \boldsymbol{I}$, where $\boldsymbol{I}$ is the unit matrix and σ_n^2 is the variance of the noise. Thus, the prior expression for the joint Gaussian distribution corresponding to observations $\boldsymbol{y}$ and $\boldsymbol{f}^*$ containing ε is as follows:

$$\begin{bmatrix} \boldsymbol{y} \\ \boldsymbol{f}^* \end{bmatrix} \sim N\left(0, \begin{bmatrix} K(\boldsymbol{X}, \boldsymbol{X}) + \sigma_n^2 \boldsymbol{I} & K(\boldsymbol{X}, \boldsymbol{X}^*) \\ K(\boldsymbol{X}, \boldsymbol{X}^*)^{\mathrm{T}} & K(\boldsymbol{X}^*, \boldsymbol{X}^*) \end{bmatrix}\right) \tag{10}$$

From the above derivation, it is clear that the kernel function of GPR contains the mean function and the covariance function. The covariance function is used to measure the degree of similarity or correlation between different samples. It is a key factor affecting the GPR prediction results and is subject to positive orbit closure semidefinite. In this study, the Gaussian radial basis function (RBF), which is the most widely used and recognized for its excellent generalization performance, is set as the covariance function as shown in Eq. (11).

$$\mathrm{cov}(\boldsymbol{x}, \boldsymbol{x}') = \exp\left[-\frac{\|\boldsymbol{x}_i - \boldsymbol{x}_j\|^2}{2\sigma_1^2}\right] \tag{11}$$

where the hyperparameter$\sigma_1$determines the performance of the covariance function, which can have an influence on the generalizability and robustness of the GPR. To solve the above problem, the maximum likelihood estimate is used for optimization of hyperparameter. The specific computational procedure can be found in the literature [43–45].

4.2. Genetic algorithm

Genetic algorithm (GA) is a method to search for the optimal solution by simulating the natural evolutionary process. GA converts the problem-solving process into a process similar to the crossover and mutation of chromosomal genes in biological evolution [46–48]. It can quickly obtain good optimization results when solving more complex combinatorial optimization problems (Fig. S2).

4.3. Evaluation metrics for prediction models

In this paper, root mean square error (RMSE), correlation coefficient (R), and variance account for (VAF), which have been widely accepted by academia, are used as evaluation metrics for prediction models. The calculation equations are as follows. The closer the RMSE is to 0, the closer the R is to 1, and the closer the VAR is to 100, the better the model prediction is.

5. Prediction and optimization

5.1. Process of GPR modelling

5.1.1. Technical route of GPR modelling

GPR is constructed to predict the UCS of TWSC and provides a basis for intelligent optimization of mix proportion in this study. 51 sets of data in table 4 are used as the data set. To better evaluate the prediction performance of the model, the original data are randomly divided into a training set and a validation set in the ratio of 8:2. 41 sets of data from the training set are used to train GPR and 10 sets of data from the validation set are used to evaluate the prediction performance of GPR. After determining the priori distribution that the mean value is 0, the σ_1 of the kernel function (RBF) are then optimized using the maximum likelihood estimate according to Section 4.1 and $\sigma_1 = 66.7451$. After determining the kernel function and hyperparameter, the posterior distribution and thus the GPR can be constructed according to Eqs. (5)–(7). Finally, the GPR for characterizing the nonlinear relationship between X_1, X_2, X_3, X_4 (curing time), and Y (UCS) is constructed (Fig. S3).

5.1.2. Relationship of variables under GPR

Four variables are set in the GPR: fly ash dosage, slag powder dosage, fineness modulus of tailings, and curing time. The relationships of variables obtained based on the GPR are shown in Fig. 11. The UCS enhances and then decreases with the increase of fly ash dosage when interacting with the other 3 variables. The UCS enhanced linearly with the increase of slag powder dosage when the slag powder dosage is interacted with other 3 variables. When the fineness modulus is interacted with the other 3 variables, the UCS increased slowly with the increase of the fineness modulus. When the curing time is interacted with the other 3 variables, the UCS enhanced rapidly with the increase of curing time.

5.1.3. Analysis of results for GPR

Fig. 12 shows the prediction results of GPR with 95% confidence band for the training set and validation set. From the Fig. 12(a), it can be seen that the R, RMSE, and VAF of the training set are 0.9982, 0.1331, and 99.6419. From the Fig. 12(b), it can be seen that the R, RMSE, and VAF of the validation set are 0.9963, 0.1753, and 99.2551. The above results show that the GPR can solve the nonlinear relationship between the affecting factors and the UCS rapidly and accurately.

5.2. Comparisons with other models

In this paper, GPR is compared with multiple nonlinear regression (MNR) based on response models, support vector regression (SVR), and extreme learning machine (ELM), which are widely used in engineering practice. To ensure the fairness of the comparison, the parameters of both SVR and ELM are optimized using GA. The optimal parameters are shown in Table 5.

Fig. 13 shows the marginal histograms of prediction results for the training set and validation set of the 4 models. For

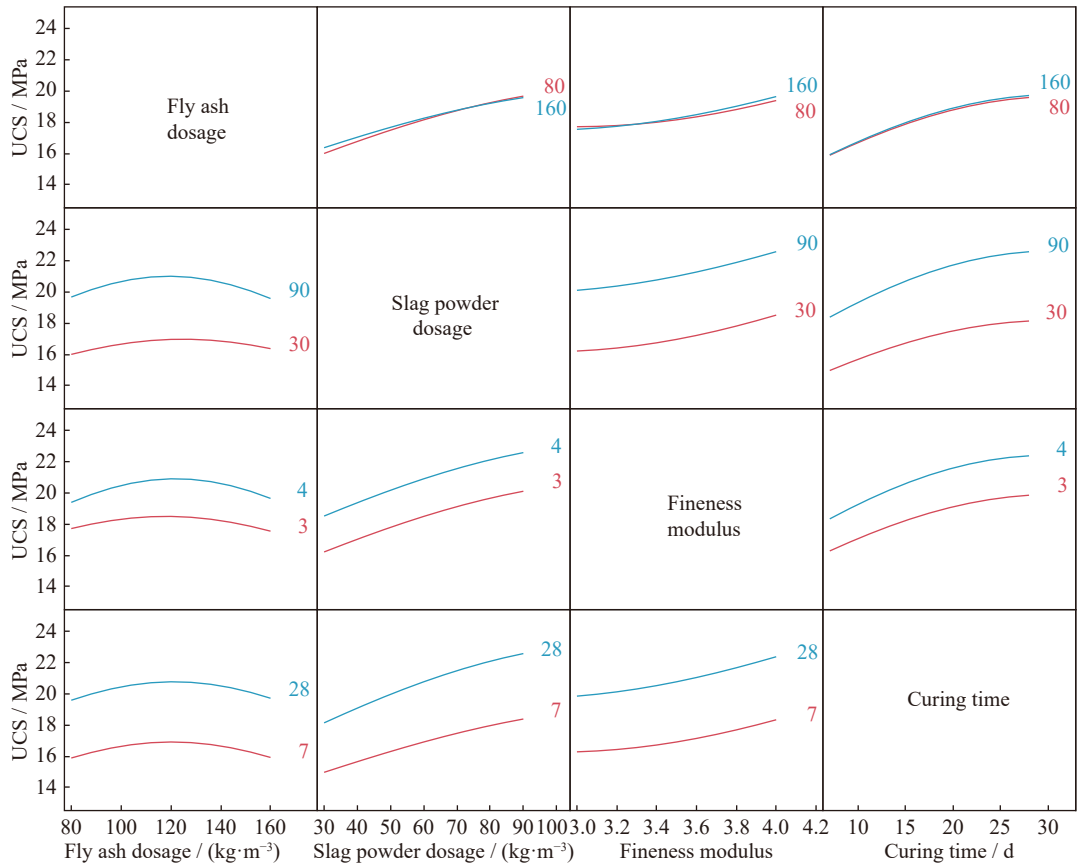

Fig. 11. Relationship of variables under GPR.

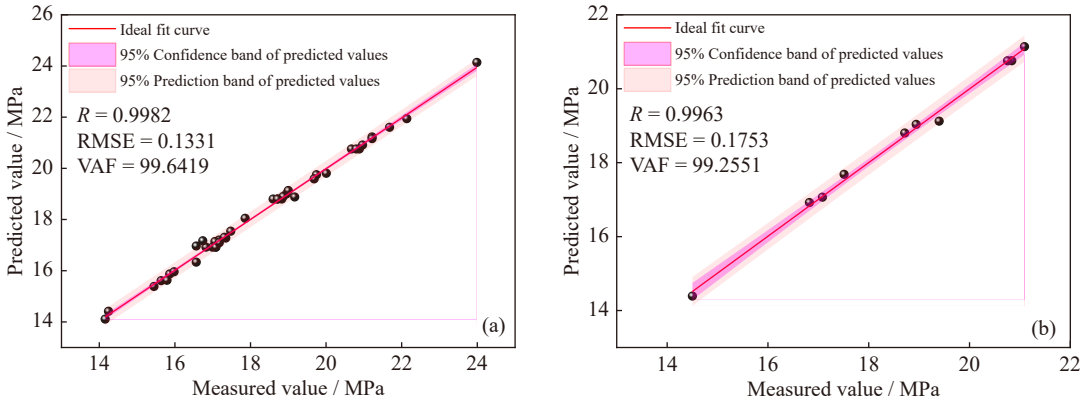

Fig. 12. GPR prediction performance of (a) training set and (b) validation set.

Table 5. Optimal parameters of SVR and ELM by using GA

SVR			ELM		
c	*g*	Max iterations	Hidden layer nodes	Learning rate	Max iterations
42.137	0.0713	117	15	0.024	163

Notes: *c* represents the regularization parameter, and *g* is the kernel coefficient.

training set, the predicted (P) and measured (M) values of the GPR largely coincide with a straight line P = M with slope 1 and *R* of 0.9982 from Fig. 13(a). This indicates that the prediction results of the training set are highly accurate and the model is excellent trained. The remaining SVR and ELM are poorly trained and have relatively large errors from Fig. 13(c) and (d). Although the *R* for training set and validation set of MNR is high (0.9956 and 0.9931) from Fig. 13(b), the multiple nonlinear regression equation has disadvantages. This is because MNR characterizes the relationship between the variables (*X*) and the response variable (*Y*) in terms of specific equations, which makes the model less robust and less generalizable. Compared to other models, GPR demonstrates the highest *R* on the validation set. Therefore, GPR accurately characterizes the nonlinear linear relationship between UCS and its affecting factors and has strong gener-

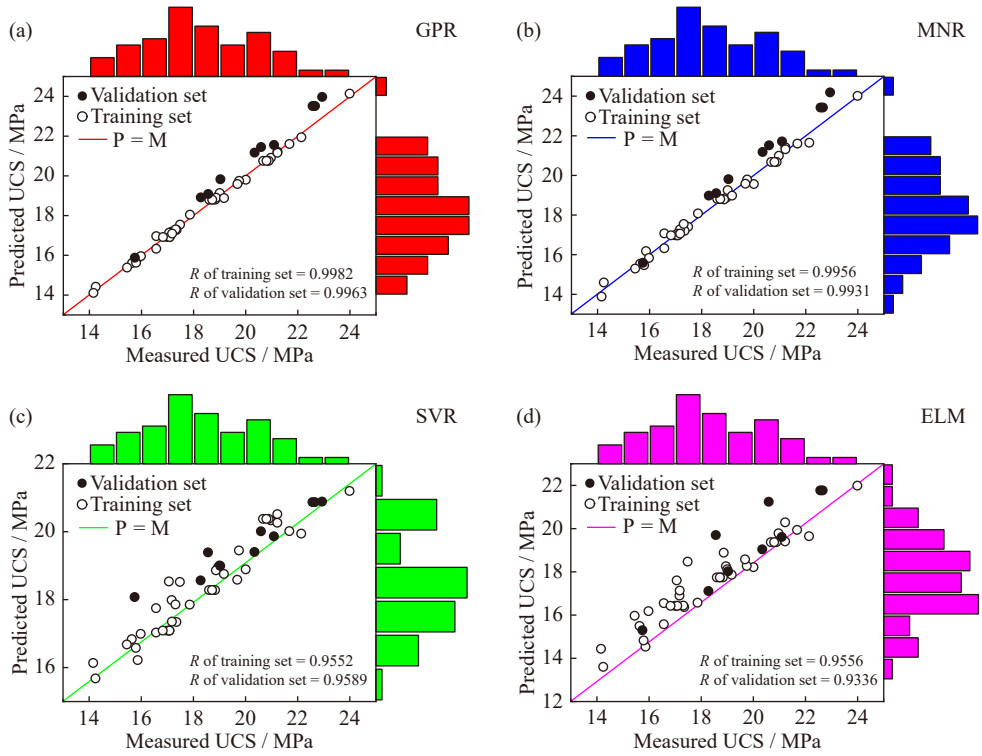

Fig. 13. Marginal histograms predicted by (a) GPR, (b) MNR, (c) SVR, and (d) ELM.

alization performance.

A ranking method for the performance of different models proposed by Zorlu *et al.* is utilized as shown in Table 6 [49]. From Table 6, the GPR has the optimal prediction performance for training set and validation set (the total rank = 12). The above analysis indicates that GPR is the optimal model to characterizing the mapping relationship between UCS and its affecting factors based on the experimental sample data in this study.

5.3. Mix proportion optimization by GPR–GA

GA is introduced to solve the optimal mix proportion of TWSC at different constraint conditions on the basis of construction of GPR in this study. Firstly, a nonlinear mapping relationship between each affecting factor and UCS is constructed using GPR (as described in Section 4.1). Secondly, the constructed GPR is considered as a nonlinear function f_{GPR} for predicting the UCS and adding constraint conditions to f_{GPR} for engineering applications (f_{GPR} is called the objective function). Finally, the above objective function is used as the fitness function in the GA and the GA is used to search for the minimum value of the fitness function. The minimum value is the optimal solution and the optimum mix proportion corresponding to this optimal solution can be obtained (Fig. S4).

The optimal mix proportions for TWSC with UCS of 15 and 20 MPa (objective functions are f_{15} and f_{20}) are solved using GPR–GA. The optimization results for mix proportions are shown in Table 7. It can be seen that the errors of predicted UCS and measured UCS for the optimized mix proportions with the target strengths of 15 and 20 MPa are 1.45% and 1.86%, respectively. This shows that the

Table 6. Performance indices of different models

Network	Results of evaluation for whole sets			Rank values			Total rank
	R	RMSE	VAF	*R*	RMSE	VAF	
GPR	0.9979	0.1433	99.5635	4	4	4	12
MNR	0.9951	0.2146	99.0216	3	3	3	9
SVR	0.9526	0.9489	80.8987	2	2	1	5
ELM	0.9108	1.0539	82.8835	1	1	2	4

Table 7. Optimization results for mix proportions of TWSC by GPR–GA

Objective function	Optimal mix proportion				Optimal mix proportion after rounding				Predicted UCS / MPa	Measured UCS / MPa	Error / %
	FAD	SPD	FM	CT	FAD	SPD	FM	CT			
f_{15}	74.59	24.58	3.04	27.88	75.00	25.00	3.00	28.00	15.39	15.17	1.45
f_{20}	96.17	56.79	3.42	27.93	96.00	57.00	3.40	28.00	20.08	20.46	1.86

Note: FAD, SPD, FM, and CT are abbreviations for fly ash dosage, slag powder dosage, fineness modulus, and curing time, respectively.

GPR–GA model can rapidly and accurately realize the mix proportion optimization of TWSC.

6. Conclusions

In order to develop solid waste resources as constituent materials for wet shotcrete, this study analyzes the effect law of different factors on the UCS of TWSC by RSM. The high accuracy prediction and optimization of the UCS of TWSC under multi-factor conditions are also achieved using machine learning. The main conclusions are as follows.

(1) The UCS of TWSC gradually increases with the increase of slag powder dosage and fineness modulus. In addition, the UCS increases firstly and then decreases with the increase of fly ash dosage. The UCS of TWSC is maximum when the fly ash dosage is 120 kg·m^{-3}.

(2) When the slag powder dosage is lower than 80 kg·m^{-3}, this factor has the most significant effect on the UCS in the middle and late stages of TWSC. When the slag powder dosage is higher than 80 kg·m^{-3}, this factor has the most significant effect on the early UCS of TWSC. Compared with the UCS in the middle and late stages, fly ash dosage has more significant effect on the early UCS.

(3) The average grey value increases by 22% and the UCS increases by 39% when the fineness modulus of tailings and slag powder dosage are increased by 33% and 200%, respectively. This indicates that the hydration products increase and the pores in TWSC decrease as the fineness modulus and slag powder dosage increase, which makes the cemented structure of TWSC more compact.

(4) Compared with MNR, SVR, and ELM, GPR has the highest prediction accuracy for the UCS of TWSC (R = 0.9979, RMSE = 0.1433, and VAF = 99.5635). In addition, the mix proportions of TWSC with different strength grades are obtained based on the GPR–GA.

(5) The results of the study have certain guiding significance for the development of wet shotcrete based on solid waste and are in line with the development direction of green mines. Also, the theoretical approach adopted in this paper can be used to guide the development of similar materials, effectively reducing the amount of experiment and improving research efficiency.

Acknowledgements

This work was financially supported by the National Key Research and Development Program of China (Nos. 2018YFC1900603 and 2018YFC0604604).

Conflict of Interest

Shenghua Yin is an editorial board member for this journal and was not involved in the editorial review or the decision to publish this article. The authors declare no potential conflict of interest, and the manuscript is approved by all authors for publication.

Supplementary Information

The online version contains supplementary material available at https://doi.org/10.1007/s12613-022-2563-8.

References

[1] Q.S. Chen, Y.B. Tao, Y. Feng, Q.L. Zhang, and Y.K. Liu, Utilization of modified copper slag activated by Na_2SO_4 and CaO for unclassified lead/zinc mine tailings based cemented paste backfill, *J. Environ. Manage.*, 290(2021), art. No. 112608.

[2] W. Sun, D. Wu, H. Liu, and C. Qu, Thermal, mechanical and ultrasonic properties of cemented tailings backfill subjected to microwave radiation, *Constr. Build. Mater.*, 313(2021), art. No. 125535.

[3] Q. Chen, Y. Tao, Q. Zhang, and C. Qi, The rheological, mechanical and heavy metal leaching properties of cemented paste backfill under the influence of anionic polyacrylamide, *Chemosphere*, 286(2022), art. No. 131630.

[4] Y.F. Hu, K.Q. Li, B. Zhang, and B. Han, Strength investigation of the cemented paste backfill in alpine regions using lab experiments and machine learning, *Constr. Build. Mater.*, 323(2022), art. No. 126583.

[5] H. Dang, Z.D. Chang, H.L. Zhou, S.H. Ma, M. Li, and J.L. Xiang, Extraction of lithium from the simulated pyrometallurgical slag of spent lithium-ion batteries by binary eutectic molten carbonates, *Int. J. Miner. Metall. Mater.*, 29(2022), No. 9, p. 1715.

[6] C. Qi, Q. Chen, X. Dong, Q. Zhang, and Z.M. Yaseen, Pressure drops of fresh cemented paste backfills through coupled test loop experiments and machine learning techniques, *Powder Technol.*, 361(2020), p. 748.

[7] A.X. Wu, Z.E. Ruan, and J.D. Wang, Rheological behavior of paste in metal mines, *Int. J. Miner. Metall. Mater.*, 29(2022), No. 4, p. 717.

[8] X. Wei, W. Ni, S. Zhang, X. Wang, J. Li, and H. Du, Influence of the key factors on the performance of steel slag–desulphurisation gypsum-based hydration–carbonation materials, *J. Build. Eng.*, 45(2022), art. No. 103591.

[9] S.H. Yin, L.M. Wang, X. Chen, and A.X. Wu, Agglomeration and leaching behaviors of copper oxides with different chemical binders, *Int. J. Miner. Metall. Mater.*, 28(2021), No. 7, p. 1127.

[10] C. Xu, W. Ni, K. Li, S. Zhang, Y. Li, and D. Xu, Hydration mechanism and orthogonal optimisation of mix proportion for steel slag–slag-based clinker-free prefabricated concrete, *Constr. Build. Mater.*, 228(2019), art. No. 117036.

[11] J.J. Li, S. Cao, E. Yilmaz, and Y.P. Liu, Compressive fatigue behavior and failure evolution of additive fiber-reinforced cemented tailings composites, *Int. J. Miner. Metall. Mater.*, 29(2022), No. 2, p. 345.

[12] S. Yin, Y. Shao, A. Wu, Y.M. Wang, and X. Chen, Expansion and strength properties of cemented backfill using sulphidic mill tailings, *Constr. Build. Mater.*, 165(2018), p. 138.

[13] D. Wu, W. Sun, S. Liu, and C. Qu, Effect of microwave heating on thermo-mechanical behavior of cemented tailings backfill, *Constr. Build. Mater.*, 266(2021), art. No. 121180.

[14] C. Qi, A. Fourie, and Q. Chen, Neural network and particle swarm optimization for predicting the unconfined compressive strength of cemented paste backfill, *Constr. Build. Mater.*, 159(2018), p. 473.

[15] S. Zhao, Q. Sui, C. Cao, *et al.*, Mechanical model of lateral fracture for the overlying hard rock strata along coal mine goaf, *Geomech. Eng.*, 27(2021), No. 1, p. 75.

[16] Y. Zhang, W. Gao, W. Ni, *et al.*, Influence of calcium hydroxide addition on arsenic leaching and solidification/stabilisation

behaviour of metallurgical-slag-based green mining fill, *J. Hazard. Mater.*, 390(2020), art. No. 122161.
[17] X.D. Zhao, H.X. Zhang, and W.C. Zhu, Fracture evolution around pre-existing cylindrical cavities in brittle rocks under uniaxial compression, *Trans. Nonferrous Met. Soc. China*, 24(2014), No. 3, p. 806.
[18] H.W. Song, A. Ahmad, F. Farooq, *et al*., Predicting the compressive strength of concrete with fly ash admixture using machine learning algorithms, *Constr. Build. Mater.*, 308(2021), art. No. 125021.
[19] G. Xue, E. Yilmaz, W. Song, and S. Cao, Fiber length effect on strength properties of polypropylene fiber reinforced cemented tailings backfill specimens with different sizes, *Constr. Build. Mater.*, 241(2020), art. No. 118113.
[20] E.M. Li, J. Zhou, X.Z. Shi, *et al*., Developing a hybrid model of salp swarm algorithm-based support vector machine to predict the strength of fiber-reinforced cemented paste backfill, *Eng. Comput.*, 37(2021), No. 4, p. 3519.
[21] D.W. Zhang, K.F. Zhao, H. Li, D.M. Wang, L.L. Wang, and G.F. Zhang, Dispersion properties of fly ash–slag powders under the different environment, *Constr. Build. Mater.*, 296(2021), art. No. 123649.
[22] S. Zhang, T. Shi, W. Ni, *et al*., The mechanism of hydrating and solidifying green mine fill materials using circulating fluidized bed fly ash–slag-based agent, *J. Hazard. Mater.*, 415(2021), art. No. 125625.
[23] P.V.R.K. Reddy and D.R. Prasad, A study on workability, strength and microstructure characteristics of graphene oxide and fly ash based concrete, *Mater. Today Proc.*, 62(2022), p. 2919.
[24] M. Zhai, J. Zhao, D. Wang, Y. Wang, and Q. Wang, Hydration properties and kinetic characteristics of blended cement containing lithium slag powder, *J. Build. Eng.*, 39(2021), art. No. 102287.
[25] V. Nilsen, L.T. Pham, M. Hibbard, A. Klager, S. Cramer, and D. Morgan, Prediction of concrete coefficient of thermal expansion and other properties using machine learning, *Constr. Build. Mater.*, 220(2019), p. 587.
[26] Y.E. Asri, M.B. Aicha, M. Zaher, and A.H. Alaoui, Prediction of compressive strength of self-compacting concrete using four machine learning technics, *Mater. Today Proc.*, 57(2022), p. 859.
[27] C.C. Qi, Q.S. Chen, A. Fourie, *et al*., Constitutive modelling of cemented paste backfill: A data-mining approach, *Constr. Build. Mater.*, 197(2019), p. 262.
[28] C. Qi and A. Fourie, Cemented paste backfill for mineral tailings management: Review and future perspectives, *Miner. Eng.*, 144(2019), art. No. 106025.
[29] Z. Yu, X.Z. Shi, X. Chen, *et al*., Artificial intelligence model for studying unconfined compressive performance of fiber-reinforced cemented paste backfill, *Trans. Nonferrous Met. Soc. China*, 31(2021), No. 4, p. 1087.
[30] J. Wu, H. Jing, Q. Yin, L. Yu, B. Meng, and S. Li, Strength prediction model considering material, ultrasonic and stress of cemented waste rock backfill for recycling gangue, *J. Clean. Prod.*, 276(2020), art. No. 123189.
[31] C. Qi, Q. Chen, and S.S. Kim, Integrated and intelligent design framework for cemented paste backfill: A combination of robust machine learning modelling and multi-objective optimization, *Miner. Eng.*, 155(2020), art. No. 106422.
[32] C. Qi, Q. Chen, A. Fourie, and Q. Zhang, An intelligent modelling framework for mechanical properties of cemented paste backfill, *Miner. Eng.*, 123(2018), p. 16.
[33] E. Barreno-Avila, E. Moya-Moya, and C. Pérez-Salinas, Rice-husk fiber reinforced composite (RFRC) drilling parameters optimization using RSM based desirability function approach, *Mater. Today Proc.*, 49(2022), p. 167.
[34] M.A. Fauzi, M.F. Arshad, N.M. Nor, and E. Ghazali, Modeling and optimization of properties for unprocessed-fly ash (u-FA) controlled low-strength material as backfill materials, *Clean. Eng. Technol.*, 6(2022), art. No. 100395.
[35] L. Zhu, Z. Jin, Y. Zhao, and Y. Duan, Rheological properties of cemented coal gangue backfill based on response surface methodology, *Constr. Build. Mater.*, 306(2021), art. No. 124836.
[36] Y. Wang, H. Zhang, Y. Tan, and J. Zhu, Sealing performance of compacted block joints backfilled with bentonite paste or a particle-powder mixture, *Soils Found.*, 61(2021), No. 2, p. 496.
[37] K.R. Vishwakarma, N.L. Richards, and M.C. Chaturvedi, Microstructural analysis of fusion and heat affected zones in electron beam welded ALLVAC® 718PLUS™ superalloy, *Mater. Sci. Eng. A*, 480(2008), No. 1-2, p. 517.
[38] J.H. Hu, F.W. Zhao, Y. Kuang, D.J. Yang, M.H. Zheng, and L. Zhao, Microscopic characteristics of the action of an air entraining agent on cemented paste backfill pores, *Alex. Eng. J.*, 59(2020), No. 3, p. 1583.
[39] J.X. Xiao, X. Li, and J.H. Shi, Local linear smoothers using inverse Gaussian regression, *Stat. Papers*, 60(2019), No. 4, p. 1225.
[40] J.Q. Shi, R. Murray-Smith, and D.M. Titterington, Bayesian regression and classification using mixtures of Gaussian processes, *Int. J. Adapt. Control Signal Process.*, 17(2003), No. 2, p. 149.
[41] J.Q. Shi, B. Wang, R. Murray-Smith, and D.M. Titterington, Gaussian process functional regression modeling for batch data, *Biometrics*, 63(2007), No. 3, p. 714.
[42] J. Dearmon and T.E. Smith, Gaussian process regression and Bayesian model averaging: An alternative approach to modeling spatial phenomena, *Geogr. Anal.*, 48(2016), No. 1, p. 82.
[43] C.H. Yu, M. Li, C. Noe, S. Fischer-Baum, and M. Vannucci, Bayesian inference for stationary points in Gaussian process regression models for event-related potentials analysis, *Biometrics*, 2022. DOI: 10.1111/biom.13621
[44] C. Demay, B. Iooss, L. Le Gratiet, and A. Marrel, Model selection based on validation criteria for Gaussian process regression: An application with highlights on the predictive variance, *Qual. Reliab. Eng. Int.*, 38(2022), No. 3, p. 1482.
[45] G. Maculotti, G. Genta, D. Quagliotti, M. Galetto, and H. Hansen, Gaussian process regression-based detection and correction of disturbances in surface topography measurements, *Qual. Reliab. Eng. Int.*, 38(2021), No. 3, p. 1501.
[46] T. Mukherjee, A. Banerjee, G. Varsamopoulos, S.K.S. Gupta, and S. Rungta, Spatio-temporal thermal-aware job scheduling to minimize energy consumption in virtualized heterogeneous data centers, *Comput. Netw.*, 53(2009), No. 17, p. 2888.
[47] A. Rezaei-Bazkiaei, E. Dehghan-Niri, E.M. Kolahdouz, A.S. Weber, and G.F. Dargush, A passive design strategy for a horizontal ground source heat pump pipe operation optimization with a non-homogeneous soil profile, *Energy Build.*, 61(2013), p. 39.
[48] V. Houšt', J. Eliáš, and L. Mič̆a, Shape optimization of concrete buried arches, *Eng. Struct.*, 48(2013), p. 716.
[49] K. Zorlu, C. Gokceoglu, F. Ocakoglu, H.A. Nefeslioglu, and S. Acikalin, Prediction of uniaxial compressive strength of sandstones using petrography-based models, *Eng. Geol.*, 96(2008), No. 3-4, p. 141.